

ARTICLE OPEN

Self-organized quantum dots in marginally twisted MoSe₂/WSe₂ and MoS₂/WS₂ bilayersV. V. Enaldiev^{1,2}✉, F. Ferreira^{1,2}, J. G. McHugh^{1,2} and Vladimir I. Fal'ko^{1,2,3}✉

Moiré superlattices in twistrionic heterostructures are a powerful tool for materials engineering. In marginally twisted (small misalignment angle, θ) bilayers of nearly lattice-matched two-dimensional (2D) crystals moiré patterns take the form of domains of commensurate stacking, separated by a network of domain walls (NoDW) with strain hot spots at the NoDW nodes. Here, we show that, for type-II transition metal dichalcogenide bilayers MoX₂/WX₂ (X=S, Se), the hydrostatic strain component in these hot spots creates quantum dots for electrons and holes. We investigate the electron/hole states bound by such objects, discussing their manifestations via the intralayer intraband infrared transitions. The electron/hole confinement, which is strongest for $\theta < 0.5^\circ$, leads to a red-shift of their recombination line producing single-photon emitters (SPE) broadly tuneable around 1 eV by misalignment angle. These self-organized dots can form in bilayers with both aligned and inverted MoX₂ and WX₂ unit cells, emitting photons with different polarizations. We also find that the hot spots of strain reduce the intralayer MoX₂ A-exciton energy, enabling selective population of the quantum dot states.

npj 2D Materials and Applications (2022)6:74; <https://doi.org/10.1038/s41699-022-00346-0>

INTRODUCTION

The formation of minibands is a common moiré superlattice (mSL) effect^{1–14}, often related to a rigid rotation of one 2D crystal against the other. In general, the approximation of a rigid interlayer twist is valid for lattice-mismatched crystals or larger twist angles, where a short mSL period prohibits the formation of energetically preferential stacking domains of the two crystals. In contrast, for marginally (small-angle) twisted bilayers of crystals with very close lattice constants, the long period of the mSL offers sufficient space for creating preferential stacking areas. That is, the energy gain due to better adhesion can surmount the cost of intralayer strain in each of the constituent crystals. The reconstruction of small-angle twisted bilayers into a network of domains¹⁵ [2H for antiparallel (AP) and 3R for parallel-oriented (P) bilayers] has been observed in various bilayers of transition metal dichalcogenides (TMDs)^{16–20}. The observed^{16–20} and theoretically modelled^{15,21,22} structures feature hexagonal (for AP) and triangular (for P) NoDW with nodes hosting few nanometer areas of “chalcogen-on-chalcogen” stacking (X_iX_b), which are hot spots of the intralayer strain.

Below we study the effects produced by these hot spots of strain in marginally twisted same-chalcogen heterobilayers MoX₂/WX₂. While domains/NoDW form in both homo- and heterobilayers, the in-plane intralayer deformations, $\mathbf{u}(\mathbf{r})$, in those two systems are qualitatively different. In homobilayers the formation of preferential stacking domains is brought about by twisting locally the crystals toward each other. As a result, the deformations at the domain walls are predominantly shear in character, that is, with $\text{div } \mathbf{u} \equiv u_{ii} \rightarrow 0$, where $u_{ij} \equiv \frac{1}{2}(\partial_j u_i + \partial_i u_j)$ is a 2D strain tensor, and u_{ii} is its trace. In perfectly aligned ($\theta = 0^\circ$) heterobilayers, lattice mismatch ($\delta \approx 0.2\%$ for MoS₂/WS₂ and $\delta \approx 0.4\%$ for MoSe₂/WSe₂) requires an adjustment of the MoX₂ ($u_{ii}^{\text{Mo}} \approx -\delta$ compression) and WX₂ ($u_{ii}^{\text{W}} \approx \delta$ expansion) lattices toward each other inside the large area

domains. This inflicts a few percent of hydrostatic compression of WX₂ and expansion of MoX₂ in X_iX_b areas (NoDW nodes), quantified in Figs. 1 and 2, which, as we demonstrate below, create deep confinement potentials for charge carriers and interlayer excitons (iXs). Theoretical modelling^{23–27} of localized iXs in WX₂/MoX₂ bilayer has been attempted earlier, however without taking into account strong lattice relaxation effects (which is applicable to structures with larger misalignment angles, $\theta > 2^\circ$). This led to the underestimation of the depth of the size of the band edge variation for electrons and holes, as compared to what we find in this Letter, and with different positioning of band edge extrema across moiré supercell. In this work we focus on small-angle twisted WX₂/MoX₂ bilayers where lattice relaxation plays the critical role on trapping charge carriers, in particular due to a substantial hydrostatic strain component at NoDW nodes. Up to now, no optical studies have been reported on such small-angle ($\theta \leq 1^\circ$) bilayers, despite that the structural features of NoDW have been demonstrated using transmission electron microscopy^{16,17} and several spectroscopic studies^{28–31} have been performed on bilayers with larger misalignment angles, where lattice reconstruction does not play such a dominant role as discussed below.

RESULTS AND DISCUSSION

Modulation of band edges by strain and charge transfer

Here, we single out the hydrostatic strain component because of the critical role it plays in determining the K-valley energies in MoX₂/WX₂ crystals. Several earlier experimental and density functional theory (DFT) studies^{32–34} have agreed that conduction and valence band edges in TMD monolayers are strongly shifted by hydrostatic strain, but without much sensitivity to shear deformations. This trend is illustrated in Fig. 1.

¹School of Physics and Astronomy, University of Manchester, Oxford Road, Manchester M13 9PL, UK. ²National Graphene Institute, University of Manchester, Oxford Road, Manchester M13 9PL, UK. ³Henry Royce Institute for Advanced Materials, University of Manchester, Oxford Road, Manchester M13 9PL, UK.

✉email: vladimir.enaldiev@manchester.ac.uk; vladimir.falko@manchester.ac.uk

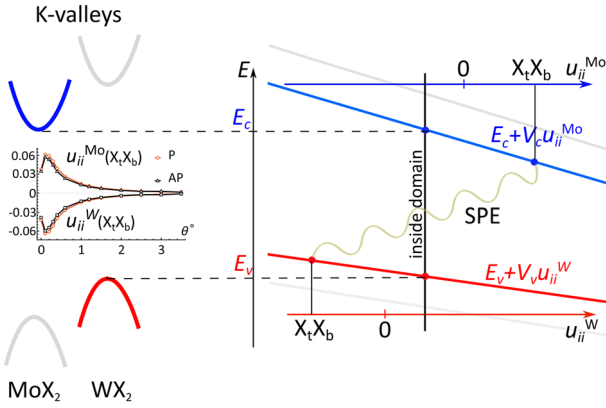


Fig. 1 Variation of K-valley conduction/valence, $E_{c/v}$, band edges in MoX_2 (blue) and WX_2 (red) monolayers under hydrostatic strain with alignment of the bands corresponding to lattice-matched WX_2/MoX_2 heterobilayers. The vertical black solid line shows the value of hydrostatic strain of individual layers inside domains. These values are opposite in sign with respect to those in $X_t X_b$ nodes, leading to formation of localized electron and hole states in self-organized QDs, which are suitable for SPE (wavy line). Inset shows twist angle dependence of hydrostatic components of strain in MoX_2 and WX_2 layers in $X_t X_b$ nodes of NoDW.

The corresponding shifts of conduction/valence band edges in MoX_2/WX_2 determine the energy of the interlayer exciton (iX). Inside domains formed by lattice reconstruction, hydrostatic strains compensate lattice mismatch between the layers: this slightly increases the band gap as compared to rigidly twisted bilayers without strain (Fig. 1). Compensating small deformations inside large domain areas, $u_{ij}^{\text{Mo,W}}$ in $X_t X_b$ nodes have the opposite signs and much larger magnitudes as compared to $u_{ij}^{\text{Mo,W}}$ inside domains. This strongly decreases layer-indirect band gap and determines deep confinement potentials for both electrons and holes, leading to the appearance of SPEs.

The intralayer strain ($u_{ij}^{\text{Mo,W}}$) maps in Fig. 2 were computed using a multiscale modelling approach¹⁵, tested in the detailed comparison with the STEM microscopy data¹⁶. This approach starts with the computation of stacking-dependent MoX_2/WX_2 adhesion energy, \mathcal{W} , followed by the parametrization of interpolation formulae¹⁵ for its dependence on the interlayer lateral offset, \mathbf{r}_0 . For both P and AP bilayers, energetically favorable stackings are those with the largest lateral separation between chalcogens. These stackings are $\text{Mo}_t X_b$ and $X_t W_b$ for P-orientation and 2H for AP-orientation. Note that $X_t X_b$ stacking is unfavorable energetically, and its interlayer distance swells¹⁵ by up to ≈ 0.5 Å. By combining interpolation formulae for $\mathcal{W}(\mathbf{r}_0)$ ¹⁵ where we use local lateral offset,

$$\mathbf{r}_0(\mathbf{r}) = \delta \cdot \mathbf{r} + \theta \hat{z} \times \mathbf{r} + \mathbf{u}^{\text{Mo}} - \mathbf{u}^{\text{W}}, \quad (1)$$

with elasticity theory and minimizing total energy of the bilayer across its mSL (which period, $\ell \approx a/\sqrt{\theta^2 + \delta^2}$, is fixed by the twist angle and lattice mismatch between the crystals), we compute the deformation fields.

In Fig. 2a, c, we present u_{ij}^{Mo} maps for $\text{MoSe}_2/\text{WSe}_2$ bilayers with $\theta = 0^\circ$ and $\theta = 0.4^\circ$, where the preferential stacking domains (triangular/hexagonal for P/AP-bilayer) are separated by networks of dislocation-like domain walls with $X_t X_b$ stacking at the NoDW nodes¹⁵. Note that for small twist angles the hydrostatic component of strain persists, now combined with shear deformations (similar to those in twisted homobilayers).

To incorporate strain into the shifts of conduction/valence band edges, $\delta E_{c/v}$ we performed DFT modelling of the TMD band structures using Quantum ESPRESSO³⁵ (see Methods).

The computed variations of all band edges can be described as $\approx V_{v/c} u_{ij}$ with $V_c^{\text{MoS}_2} = -12.45$ eV, $V_v^{\text{WS}_2} = -5.94$ eV, $V_c^{\text{MoSe}_2} = -11.57$ eV, $V_v^{\text{WSe}_2} = -5.76$ eV, which are quoted for the relevant bilayer bands. Using these values, we compute,

$$\delta E_{v/c}(\mathbf{r}) = V_{v/c} u_{ij}^{\text{W/Mo}}(\mathbf{r}) - e\phi_{\text{piezo}}^{\text{W/Mo}}(\mathbf{r}) \pm \frac{1}{2} \Delta(\mathbf{r}), \quad (2)$$

taking into account strain-dependent piezoelectric potential¹⁵, $-e\phi_{\text{piezo}}^{\text{W/Mo}}(\mathbf{r})$, and offset-dependent potential drop, $\Delta(\mathbf{r})$, due to interlayer charge transfer (for details see Supplementary Section 1). The first term in Eq. (2) represents the effect of hydrostatic component of the intralayer strain which was missed in the previous analysis of the same systems³⁶. The twist-angle dependences of the computed band edge energies $\delta E_{c/v}$ for three selected stacking areas ($\text{Mo}_t X_b$, $X_t W_b$, $X_t X_b$ for P and 2H, $\text{Mo}_t W_b$, $X_t X_b$ for AP) are plotted in Fig. 2(b). These figures suggest that $X_t X_b$ regions are potential wells for electrons and holes and these wells are the deepest for $\theta \approx \delta$. Based on that we describe the NoDW nodes as trigonally warped quantum dots (QDs), with band edge profiles exemplified in Fig. 3. These QDs are sufficiently deep to accommodate at least two size-quantized states for electrons/holes which retain their distinct s ($L_z = 0$) and p ($L_z = \pm 1$) characteristics due to the \hat{C}_3 -symmetry of the dots.

Note that QD formation in marginally twisted structures qualitatively differs from band energy profiles in stronger misaligned P-bilayers with $\theta \geq 2^\circ$, where the band edges at K-valley shift into $\text{Mo}_t X_b$ stacking areas, see Fig. 4. This crossover agrees with the findings of Refs. 23,37. In addition, for MoS_2/WS_2 with $\theta \approx 1.8^\circ$ and $\text{MoSe}_2/\text{WSe}_2$ with $\theta \approx 2.4^\circ$ the energy profile for interlayer interband exciton resembles an antidot superlattice more than an array of QDs. This contrasts with the persistence up to $\theta \sim 3.5^\circ$ of shallow QD arrays for both electrons and holes based at $X_t X_b$ areas in AP-bilayers.

Spectral characteristics of self-organized QDs

Spectral features of the interlayer interband emissions of self-organized QDs of marginally twisted bilayers are sketched on the bottom insets in Fig. 3. Energy separation, δE , between the QD transition and the iX inside the domains was computed as,

$$\delta E = \varepsilon_e^{(s)} - \varepsilon_h^{(s)} - E_{iX} - \int \int d^2 \mathbf{r} d^2 \mathbf{r}' \left| \psi_e^{(s)}(\mathbf{r}) \right|^2 \left| \psi_h^{(s)}(\mathbf{r}') \right|^2 V_{eh}(\mathbf{r} - \mathbf{r}'). \quad (3)$$

Here, E_{iX} is the iX energy and $\varepsilon_{e/h}^{(s)}$ are the energies of the electron/hole s -states $\psi_{e/h}^{(s)}$ inside quantum well. We also take into account the interlayer e-h attraction, V_{eh} , screened by the in-plane susceptibility of TMDs and hBN environment³⁸ (see details in Supplementary Sections 2 and 3). The computed dependences of $\delta E(\theta)$ for MoX_2/WX_2 bilayers ($X = \text{Se}, \text{S}$) are shown in Fig. 5. We find that the QD line can be tuned across a 0.8–1.2 eV spectral interval (telecom range) for $0.3^\circ \leq \theta \leq 1^\circ$ in $\text{MoSe}_2/\text{WSe}_2$ and for $0^\circ \leq \theta \leq 0.5^\circ$ in MoS_2/WS_2 . In Fig. 5 the computed data for electrons in AP- MoS_2/WS_2 are terminated at $\theta = 0.6^\circ$, because for a larger misalignment the K-valley conduction band profile starts resembling an antidot lattice with maxima at the 2H domains (see Fig. 2(b)).

Polarization and spin selection rules

Additional information, displayed in Fig. 3 and gathered in Table 1, concerns the polarizations of SPEs and iXs inside domains and fine structure related to a Δ_{50} -splitting^{39–43} between the spin-flip and spin-conserving interband transitions inside the QDs. We note that, in each of the two \pm K-valleys, the hole spin at the band edge is determined by the spin-valley locking in WX_2 , whereas conduction band in MoX_2 is characterized by spin-orbit splitting Δ_{50} . Also, the

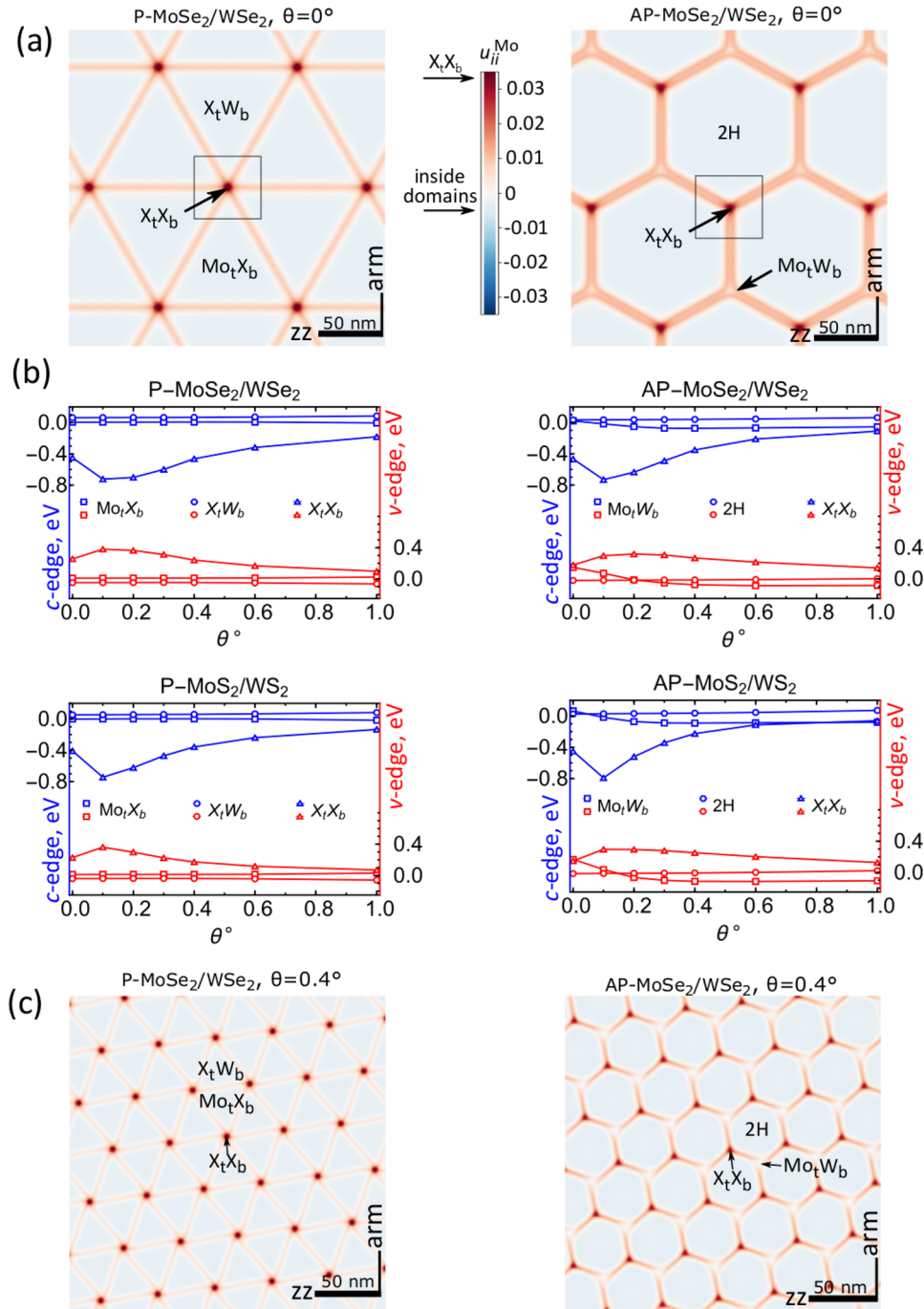


Fig. 2 Lattice reconstruction and local conduction and valence band edge modulations at K-valleys in twisted MoX₂/WX₂ bilayers. **a** and **c** Show distribution of the hydrostatic strain, u_{ij}^{Mo} , in MoSe₂ layer of P- and AP-MoSe₂/WSe₂ bilayers with $\theta = 0^\circ$ and $\theta = 0.4^\circ$, respectively. Squares in **(a)** show areas used to plot band edge profile in Fig. 3. Arrows on the scalebar indicate the values of u_{ij}^{Mo} inside domains and at NoDW nodes. **b** Modulations of conduction (c) and valence (v) band edges as a function of twist angle for high symmetry stackings of moiré supercell, indicated by different symbols, for P/AP- MoSe₂/WSe₂ and MoS₂/WS₂ bilayers. Matching MoX₂ and WX₂ lattices inside the large area domains determines homogeneous strain which is accounted for through offsetting of MoX₂ and WX₂ strain axes in Fig. 1.

iX emission from the inner part of domains, shown in Fig. 3, differs for P and AP bilayers. For AP-bilayers we expect a single line of circularly polarized iX emission. For P-bilayers iX energies and polarizations are different for Mo_tX_b and X_tW_b domains, with the energy splitting determined by the interlayer charge transfer^{36,44,45} and circular (in Mo_tX_b) vs linear (in X_tW_b) polarization, established in Ref.⁴⁶. In Table 1 we

underline the most prominent SPE transition which happens to be related to the spin-conserving recombination in self-organized QDs in P-bilayers with approximately one hundred times weaker intensity than that of intralayer A-exciton (AX) in MoX₂ layer determined by the ratio of corresponding interband matrix elements. To mention, DFT modelling suggests that lattice matching inside domains promotes direct-to-indirect

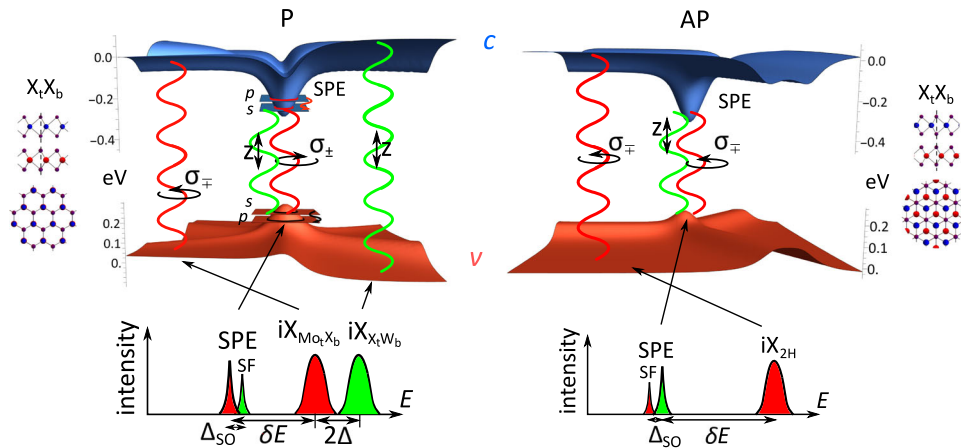


Fig. 3 Self-organized quantum dots and spectral features of SPE and iX. (Top) Conduction (c) and valence (v) band edge profiles in vicinity of $X_t X_b$ nodes of NoDW in reconstructed P- and AP-MoX₂/WX₂ bilayers with $\theta = 0^\circ$. Colors of wavy lines encode polarizations of emitted light in $\pm K$ -valleys: red for circular and green for z-polarization. Upper/lower subscript of circular polarization (σ_\pm or σ_\mp) indicates helicity of light emitted in $+K/-K$ -valleys. Left and right bottom panels show sketches of predicted optical spectra in marginally twisted P- and AP-MoX₂/WX₂ bilayers, respectively.

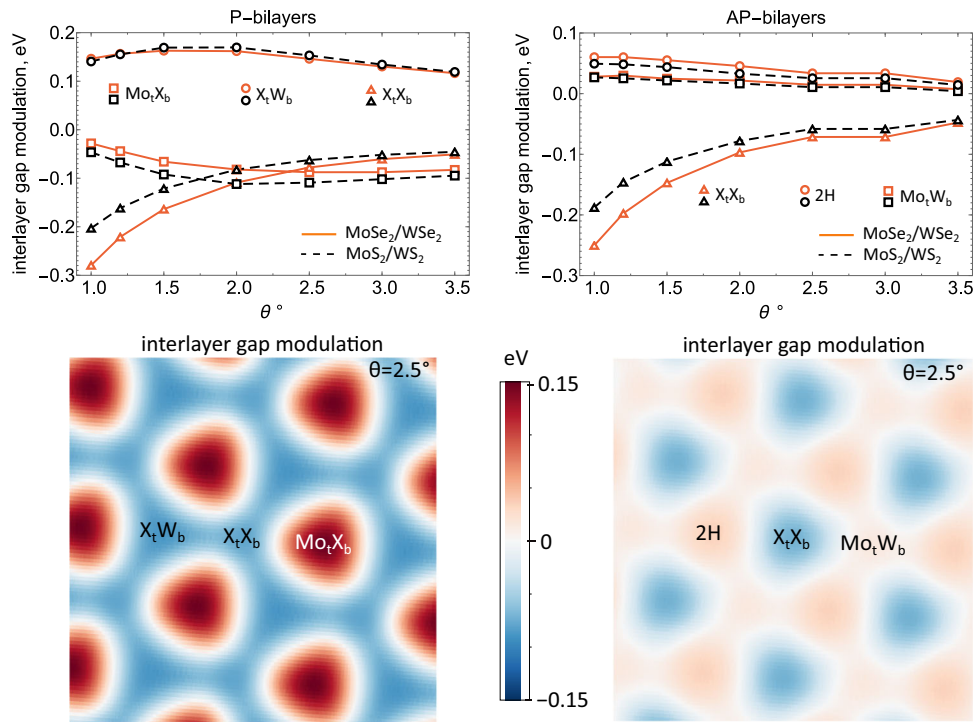


Fig. 4 (Top) Twist-angle-dependences of interlayer band gap at K-valleys at high symmetry stacking areas of moiré supercells of P- and AP-MoX₂/WX₂ bilayers with $1^\circ \leq \theta \leq 3.5^\circ$. For P-bilayers with $\theta \geq 2^\circ$, we find a crossover from an array of QDs located in $X_t X_b$ nodes to an antidot array with shallow minima at $X_t W_b$ areas and high peaks at $Mo_t X_b$ areas, while for AP-bilayers there is no such transition. (Bottom) Real space maps showing crossover (toward larger misalignment) of the interlayer band gap for MoS₂/WS₂ bilayers with $\theta = 2.5^\circ$: an antidot array for P-bilayers and shallow QD array for AP-bilayers.

band gap crossover for electrons toward Q-valley and most importantly for holes toward Γ -valley⁴⁷ (see also Supplementary Section 6).

Intralayer transitions in self-organized QDs

In addition, intraband $s-p$ optical transitions for electrons/holes trapped in QDs give rise to infrared (IR) features with energies shown in Fig. 6(a) for twist angles $0^\circ \leq \theta \leq 1^\circ$. In AP-bilayers, $X_t X_b$ NoDW nodes also feature spikes of pseudomagnetic field B^* ¹⁵

characteristic of multivalley semiconductors with a strongly inhomogeneous strain^{48–50}. These pseudomagnetic fields have opposite signs for electrons in $\pm K$ -valleys, splitting (by $\hbar\Delta v = 5 \mu_B B^*$) the QD $s-p$ transitions into circularly polarized doublets, as sketched in Fig. 6(a). Such an IR transition can be used to manipulate the state of the SPE, by exciting either electron or hole into their respective QD p -states.

The intralayer band gap variation, due to the hydrostatic strain at $X_t X_b$ nodes reduces/increases the energy of the intralayer AX in

MoX₂/WX₂. In Fig. 6(b) we show that this results in a ~100 meV potential well for AX in MoX₂ exactly over the self-organized QD position. The red-shift of the MoX₂ AX confined in such a well can be used for selective population of the QD states, upon the relaxation of photoexcited hole in MoX₂ layer into its bound state in the QD in WX₂.

Discussion

Overall, hot spots of hydrostatic strain at the nodes of domain wall network, generated by the lattice reconstruction in marginally twisted MoX₂/WX₂ bilayers, form a nanoscale array of QDs for electrons and holes, which may be operated as single-photon emitters. Based on the presented analysis, we propose that the SPE spectrum can be tuned by the choice of the twist angle over a broad range (including telecom for MoSe₂/WSe₂ bilayers), and the electron/hole state in these QDs can be manipulated via intra-band *s*–*p* transitions using THz radiation. The data on the optical oscillator strength of the interlayer interband transitions in such QDs, Table 1, suggest that the brightest would be SPEs in marginally twisted bilayers with parallel orientation of MoX₂ and WX₂ unit cells. Ratio of intra- and inter-layer interband velocity matrix elements also suggest that the recombination rate of QD-localized excitons is about ~1% of the recombination rate of the intralayer A-exciton in MoX₂; as the latter was found in Refs. ^{51–54} to be

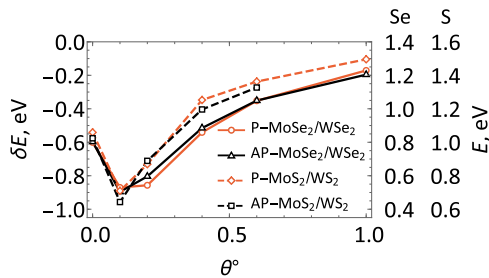


Fig. 5 Energies of SPEs in P/AP-WX₂/MoX₂ bilayers shown as a shift from the lower iX energy inside the domains (left-side axis common for all bilayers) and as an absolute value (right-side axis specified separately for selenides and sulfides). The latter were determined as $E = \delta E + 1.4$ eV and $E = \delta E + 1.6$ eV for selenide (Se) and sulfide (S), respectively. These estimates are based on calculated binding energies of iXs ≈ 65 meV (see details in Supplementary Section 2) and measured positions of photoluminescence peaks of iXs in MoSe₂/WSe₂³⁰ and MoS₂/WS₂⁴⁷.

$\sim 1/300 - 1/200$ fs⁻¹, this would set a 100 MHz possible repetition rate for SPEs in these self-organized QDs. Note that areal density of these SPEs is $\sim 10^{11}$ cm⁻², which is 100 times higher than the density of quantum emitters in patterned TMD monolayers^{55,56} and that a red-shift of the A-exciton in MoX₂,

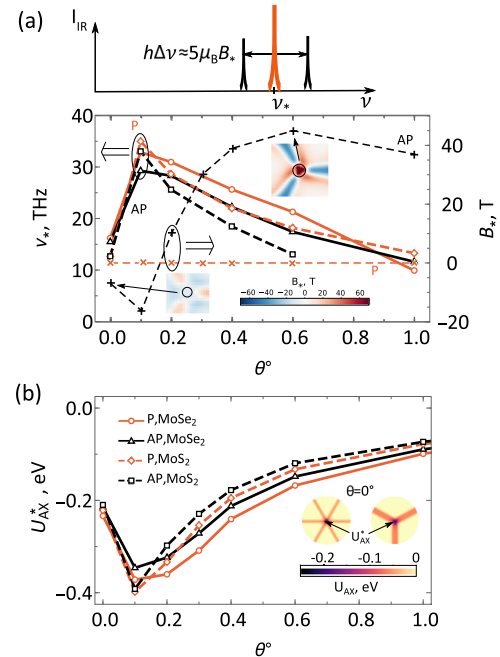


Fig. 6 QD characteristics for electrons and holes. Intralayer infrared features of QDs and intralayer (MoX₂) band gap variation with marking of materials and orientations of the bilayers shown on (b). **a** Infrared line, ν_* , of a QD in P- and AP-MoX₂/WX₂ bilayers, with a line splitting due to pseudomagnetic field, B_* , in AP-structures. Twist angle dependence of QD *s*–*p*-transition frequency was analyzed based on Eq. (2) and B_* was estimated for conduction band electrons in MoS₂ using parameters from Ref. ⁵⁰. Pseudomagnetic field maps around $X_t X_b$ nodes of NoDW for $\theta = 0^\circ$ and $\theta = 0.6^\circ$ are shown in the insets. Pseudomagnetic fields of similar magnitude are expected for holes in MoS₂/WS₂ bilayers and both electrons and holes for MoSe₂/WSe₂ bilayers. **b** Depth of a potential well, U_{AX}^* , confining intralayer A-excitons in MoX₂, created by hydrostatic strain around $X_t X_b$ nodes of NoDW. Inset shows anisotropy of the well profile for P- and AP-MoSe₂/WSe₂ bilayers with $\theta = 0^\circ$.

Table 1. Polarization of emitted photons by SPE, iX and AX in MoX₂, and strength of the emission characterized by interband velocity matrix element, $|v_{\pm,z}^{cv}|$ (in $10^6 \times \text{cm/s}$, $v_{\pm} = v_x \pm i v_y$) computed with Quantum ESPRESSO (for details see Supplementary Sections 4 and 5).

	AX MoX ₂	P-SPE _{X_tX_b}	P-iX _{Mo_tX_b}	P-iX _{X_tW_b}	AP-SPE _{X_tX_b}	AP-iX _{2H}
Ground (<i>E</i>)	Spin-conserving				Spin-flip	
	σ_{\pm}	σ_{\pm}	σ_{\mp}	<i>z</i>	σ_{\mp}	σ_{\pm}
S	113	<u>6.42</u>	4.57	2.53	0.48	2.28
Se	97	<u>7.03</u>	5.30	3.73	0.54	3.49
Excited (<i>E</i> + Δ _{SO})	Spin-flip				Spin-conserving	
		<i>z</i>	σ_{\pm}	σ_{\mp}	<i>z</i>	σ_{\mp}
S		0.49	2.82	0.12	1.18	10.30
Se		0.74	5.01	0.10	1.89	10.64

$\sigma+$ ($\sigma-$) designates photons with clockwise (counter clockwise) polarization outgoing in positive direction of spin quantization axis. *z* stands for linear out-of-plane polarization. Here, upper (lower) index corresponds to emission from +K (–K) valley. For this analysis we employed angular momentum conservation for K-point Bloch states (we used center of coordinate set at a chalcogen atom).

due to the same hot spots of strain, would enable selective population of the QD states for the optical pumping of the self-organized SPEs.

Finally, we note that in real samples there is usually inhomogeneity of domain structure caused by smooth strain introduced during sample transfer process. Such inhomogeneity spread a spectral range of SPEs available on a single wafer, which can be used to produce a wealth of SPE devices operating in complementary spectral intervals provided by different parts of a single large-area WX_2/MoX_2 bilayer.

METHODS

Computation of hydrostatic strain effect

To quantify effect of hydrostatic strain on the band edges of TMD monolayers we considered biaxial strain in the range of $\pm 2\%$, fully relaxing atomic positions in the monolayer with Vanderbilt PBE GBRV ultrasoft pseudopotentials⁵⁷, a wavefunction cut-off of $E_{cut} = 50$ Ry, and a $20 \times 20 \times 1$ k -point grid, sampled according to the Monkhorst-Pack algorithm⁵⁸. Spin-orbit coupling was included by a norm-conserving fully-relativistic pseudopotential (We used the relevant relativistic pseudopotentials from <http://www.quantum-espresso.org>.) with $E_{cut} = 80$ Ry.

DATA AVAILABILITY

The data that support the plots in the paper are available from the corresponding authors upon reasonable request.

Received: 13 April 2022; Accepted: 27 September 2022;

Published online: 23 October 2022

REFERENCES

- Cao, Y. et al. Correlated insulator behaviour at half-filling in magic-angle graphene superlattices. *Nature* **556**, 80 (2018).
- Cao, Y. et al. Unconventional superconductivity in magic-angle graphene superlattices. *Nature* **556**, 43 (2018).
- Yankowitz, M. et al. Tuning superconductivity in twisted bilayer graphene. *Science* **363**, 1059–1064 (2019).
- Lu, X. et al. Superconductors, orbital magnets and correlated states in magic-angle bilayer graphene. *Nature* **574**, 653–657 (2019).
- Xu, S. et al. Tunable van Hove singularities and correlated states in twisted monolayer–bilayer graphene. *Nat. Phys.* **17**, 619–626 (2021).
- Sharpe, A. L. et al. Emergent ferromagnetism near three-quarters filling in twisted bilayer graphene. *Science* **365**, 605–608 (2019).
- Polshyn, H. et al. Electrical switching of magnetic order in an orbital Chern insulator. *Nature* **588**, 66–70 (2020).
- Chen, G. et al. Evidence of a gate-tunable Mott insulator in a trilayer graphene moiré superlattice. *Nat. Phys.* **15**, 237–241 (2019).
- Chen, S. et al. Electrically tunable correlated and topological states in twisted monolayer–bilayer graphene. *Nat. Phys.* **17**, 374–380 (2021).
- Shen, C. et al. Correlated states in twisted double bilayer graphene. *Nat. Phys.* **16**, 520–525 (2020).
- Park, J. M., Cao, Y., Watanabe, K., Taniguchi, T. & Jarillo-Herrero, P. Tunable strongly coupled superconductivity in magic-angle twisted trilayer graphene. *Nature* **590**, 249–255 (2021).
- Cao, Y. et al. Nematicity and competing orders in superconducting magic-angle graphene. *Science* **372**, 264–271 (2021).
- Liu, X. et al. Tunable spin-polarized correlated states in twisted double bilayer graphene. *Nature* **583**, 221–225 (2020).
- Gadelha, A. C. et al. Localization of lattice dynamics in low-angle twisted bilayer graphene. *Nature* **590**, 405–409 (2021).
- Enaldiev, V. V., Zólyomi, V., Yelgel, C., Magorrian, S. J. & Fal'ko, V. I. Stacking domains and dislocation networks in marginally twisted bilayers of transition metal dichalcogenides. *Phys. Rev. Lett.* **124**, 206101 (2020).
- Weston, A. et al. Atomic reconstruction in twisted bilayers of transition metal dichalcogenides. *Nat. Nanotechnol.* **15**, 592–597 (2020).
- Rosenberger, M. R. et al. Twist angle-dependent atomic reconstruction and moiré patterns in transition metal dichalcogenide heterostructures. *ACS Nano* **14**, 4550–4558 (2020).
- Sung, J. et al. Broken mirror symmetry in excitonic response of reconstructed domains in twisted $MoSe_2/MoSe_2$ bilayers. *Nat. Nanotechnol.* **15**, 750–754 (2020).
- McGilly, L. J. et al. Visualization of moiré superlattices. *Nat. Nanotechnol.* **15**, 580–584 (2020).
- Shabani, S. et al. Deep moiré potentials in twisted transition metal dichalcogenide bilayers. *Nat. Phys.* **17**, 720–725 (2021).
- Naik, M. H. & Jain, M. Ultraflatbands and shear solitons in moiré patterns of twisted bilayer transition metal dichalcogenides. *Phys. Rev. Lett.* **121**, 266401 (2018).
- Carr, S. et al. Relaxation and domain formation in incommensurate two-dimensional heterostructures. *Phys. Rev. B* **98**, 224102 (2018).
- Yu, H., Liu, G.-B., Tang, J., Xu, X. & Yao, W. Moiré excitons: from programmable quantum emitter arrays to spin-orbit-coupled artificial lattices. *Sci. Adv.* **3**, e1701696 (2017).
- Wu, F., Lovorn, T. & MacDonald, A. H. Theory of optical absorption by interlayer excitons in transition metal dichalcogenide heterobilayers. *Phys. Rev. B* **97**, 035306 (2018).
- Lu, X., Li, X. & Yang, L. Modulated interlayer exciton properties in a two-dimensional moiré crystal. *Phys. Rev. B* **100**, 155416 (2019).
- Brem, S., Linderäl, C., Erhart, P. & Malic, E. Tunable phases of moiré excitons in van der Waals heterostructures. *Nano Lett.* **20**, 8534–8540 (2020).
- Guo, H., Zhang, X. & Lu, G. Shedding light on moiré excitons: a first-principles perspective. *Sci. Adv.* **6**, eabc5638 (2020).
- Tran, K. et al. Evidence for moiré excitons in van der Waals heterostructures. *Nature* **567**, 71–75 (2019).
- Seyler, K. L. et al. Signatures of moiré-trapped valley excitons in $MoSe_2/WSe_2$ heterobilayers. *Nature* **567**, 66–70 (2019).
- Baek, H. et al. Highly energy-tunable quantum light from moiré-trapped excitons. *Sci. Adv.* **6**, eaba8526 (2020).
- Brotos-Gisbert, M. et al. Spin-layer locking of interlayer excitons trapped in moiré potentials. *Nat. Mater.* **19**, 630–636 (2020).
- Conley, H. J. et al. Bandgap engineering of strained monolayer and bilayer MoS_2 . *Nano Lett.* **13**, 3626–3630 (2013).
- Dhakal, K. P. et al. Local strain induced band gap modulation and photoluminescence enhancement of multilayer transition metal dichalcogenides. *Chem. Mater.* **29**, 5124–5133 (2017).
- Zollner, K., Junior, P. E. F. & Fabian, J. Strain-tunable orbital, spin-orbit, and optical properties of monolayer transition-metal dichalcogenides. *Phys. Rev. B* **100**, 195126 (2019).
- Giannozzi, P. et al. Quantum espresso: a modular and open-source software project for quantum simulations of materials. *J. Phys.: Condensed Matter* **21**, 395502 (19pp) (2009).
- Enaldiev, V. V., Ferreira, F., Magorrian, S. J. & Fal'ko, V. I. Piezoelectric networks and ferroelectric domains in twistronic superlattices in WS_2/MoS_2 and $WSe_2/MoSe_2$ bilayers. *2D Mater.* **8**, 025030 (2021).
- Brem, S., Linderäl, C., Erhart, P. & Malic, E. Tunable phases of moiré excitons in van der Waals heterostructures. *Nano Lett.* **20**, 8534–8540 (2020).
- Danovich, M. et al. Localized interlayer complexes in heterobilayer transition metal dichalcogenides. *Phys. Rev. B* **97**, 195452 (2018).
- Mak, K. F., He, K., Shan, J. & Heinz, T. F. Control of valley polarization in monolayer MoS_2 by optical helicity. *Nat. Nanotechnol.* **7**, 494–498 (2012).
- Echeverry, J. P., Urbaszek, B., Amand, T., Marie, X. & Gerber, I. C. Splitting between bright and dark excitons in transition metal dichalcogenide monolayers. *Phys. Rev. B* **93**, 121107 (2016).
- Wang, G. et al. In-plane propagation of light in transition metal dichalcogenide monolayers: Optical selection rules. *Phys. Rev. Lett.* **119**, 047401 (2017).
- Liu, G.-B., Shan, W.-Y., Yao, Y., Yao, W. & Xiao, D. Three-band tight-binding model for monolayers of group-VIB transition metal dichalcogenides. *Phys. Rev. B* **88**, 085433 (2013).
- Kormányos, A. et al. k -p theory for two-dimensional transition metal dichalcogenide semiconductors. *2D Mater.* **2**, 022001 (2015).
- Ferreira, F., Enaldiev, V. V., Fal'ko, V. I. & Magorrian, S. J. Weak ferroelectric charge transfer in layer-asymmetric bilayers of 2D semiconductors. *Sci. Rep.* **11**, 13422 (2021).
- Weston, A. et al. Interfacial ferroelectricity in marginally twisted 2D semiconductors. *Nat. Nanotechnol.* **17**, 390–395 (2022).
- Yu, H., Liu, G.-B. & Yao, W. Brightened spin-triplet interlayer excitons and optical selection rules in van der Waals heterobilayers. *2D Mater.* **5**, 035021 (2018).
- Kiemle, J. et al. Control of the orbital character of indirect excitons in MoS_2/WSe_2 heterobilayers. *Phys. Rev. B* **101**, 121404 (2020).
- Lordanskii, S. V. & Koshelev, A. E. Dislocations and localization effects in multivalley conductors. *JETP Lett.* **41**, 471 (1985).

49. Suzuura, H. & Ando, T. Phonons and electron-phonon scattering in carbon nanotubes. *Phys. Rev. B* **65**, 235412 (2002).
50. Rostami, H., Roldán, R., Cappelluti, E., Asgari, R. & Guinea, F. Theory of strain in single-layer transition metal dichalcogenides. *Phys. Rev. B* **92**, 195402 (2015).
51. Poellmann, C. et al. Resonant internal quantum transitions and femtosecond radiative decay of excitons in monolayer WSe₂. *Nat. Mater.* **14**, 889–893 (2015).
52. Dey, P. et al. Optical coherence in atomic-monolayer transition-metal dichalcogenides limited by electron-phonon interactions. *Phys. Rev. Lett.* **116**, 127402 (2016).
53. Jakubczyk, T. et al. Radiatively limited dephasing and exciton dynamics in MoSe₂ monolayers revealed with four-wave mixing microscopy. *Nano Lett.* **16**, 5333–5339 (2016).
54. Cadiz, F. et al. Excitonic linewidth approaching the homogeneous limit in MoS₂-based van der Waals heterostructures. *Phys. Rev. X* **7**, 021026 (2017).
55. Palacios-Berraquero, C. et al. Large-scale quantum-emitter arrays in atomically thin semiconductors. *Nat. Commun.* **8**, 15093 (2017).
56. Luo, Y. et al. Deterministic coupling of site-controlled quantum emitters in monolayer WSe₂ to plasmonic nanocavities. *Nat. Nanotechnol.* **13**, 1137–1142 (2018).
57. Garrity, K. F., Bennett, J. W., Rabe, K. M. & Vanderbilt, D. Pseudopotentials for high-throughput DFT calculations. *Comput. Mater. Sci.* **81**, 446–452 (2014).
58. Monkhorst, H. J. & Pack, J. D. Special points for Brillouin-zone integrations. *Phys. Rev. B* **13**, 5188–5192 (1976).

ACKNOWLEDGEMENTS

This work was supported by EC-FET European Graphene Flagship Core3 Project, EC-FET Quantum Flagship Project 2D-SIPC, EPSRC grants EP/S030719/1 and EP/V007033/1, and the Lloyd Register Foundation Nanotechnology Grant.

AUTHOR CONTRIBUTIONS

V.I.F. conceived the project. Theoretical analysis was done by V.V.E., F.F., and J.G.M. All the authors discussed the results and wrote the paper.

COMPETING INTERESTS

The authors declare no competing interests.

ADDITIONAL INFORMATION

Supplementary information The online version contains supplementary material available at <https://doi.org/10.1038/s41699-022-00346-0>.

Correspondence and requests for materials should be addressed to V. V. Enaldiev or Vladimir I. Fal'ko.

Reprints and permission information is available at <http://www.nature.com/reprints>

Publisher's note Springer Nature remains neutral with regard to jurisdictional claims in published maps and institutional affiliations.



Open Access This article is licensed under a Creative Commons Attribution 4.0 International License, which permits use, sharing, adaptation, distribution and reproduction in any medium or format, as long as you give appropriate credit to the original author(s) and the source, provide a link to the Creative Commons license, and indicate if changes were made. The images or other third party material in this article are included in the article's Creative Commons license, unless indicated otherwise in a credit line to the material. If material is not included in the article's Creative Commons license and your intended use is not permitted by statutory regulation or exceeds the permitted use, you will need to obtain permission directly from the copyright holder. To view a copy of this license, visit <http://creativecommons.org/licenses/by/4.0/>.

© The Author(s) 2022